Indian J Phys
https://doi.org/10.1007/s12648-025-03783-x

ORIGINAL PAPER

Computational insights into optoelectronic, thermodynamic, and thermoelectric properties of $CsLaO_2$, $HgMgO_2$, $KInO_2$, and $RbInO_2$ Delafossite Oxides

M E Ketfi[1]*, S Saad Essaoud[2,3]*, S M Al Azar[4] and A Y Al-Reyahi[5]

[1]Department of Electronics, Faculty of Technology, University of M'sila, University Pole, Road Bordj Bou Arreridj, 28000 M'sila, Algeria

[2]Department of Physics, Faculty of Sciences, University of M'sila, University Pole, Road Bordj Bou Arreridj, 28000 M'sila, Algeria

[3]Laboratory of Materials and Renewable Energy, Faculty of Science, University of M'sila, PO Box 166 Ichebilia, 28000 M'sila, Algeria

[4]Department of Physics, Faculty of Science, Zarqa University, Zarqa 13132, Jordan

[5]Department of Physics, Faculty of Science, The Hashemite University, P. O. Box 330127, Zarqa 13133, Jordan

Received: 23 March 2025 / Accepted: 26 August 2025

Abstract: In this study, the optoelectronic, structural, thermal and thermoelectric properties of $CsLaO_2$, $HgMgO_2$, $KInO_2$, and $RbInO_2$ were investigated based on density functional theory incorporated in the Wien2K code, the semi-classical Boltzmann approximation integrated in the BoltzTraP program, and the quasi-harmonic Debye model implemented in the Gibbs2 program. The four compounds exhibit semiconductor character with indirect band gaps: 3.97 eV (Γ-A) for $KInO_2$, 4 eV (Γ-H) for $RbInO_2$, 2.82 eV (M-L) and $CsLaO_2$ and 0.3 eV (Γ-A) for HgMgO2. The effect of temperature on the heat capacity, thermal expansion coefficient, and entropy and lattice thermal conductivity was also studied. Furthermore, the optical properties of the studied compounds, including reflection and refractive coefficients, optical conductivity, and the optical absorption coefficient, were investigated to ascertain their suitability for use in photovoltaic applications. Furthermore, this study investigated the dependence of the thermoelectric parameters, including the Seebeck coefficient, electrical conductivity, electronic thermal conductivity, and factor of merit, on temperature and electron/hole concentration.

Keywords: TB-mBJ; Delafossite; Seebeck coefficient; Optoelectronics devices; Electrical and thermal conductivity coefficients; Figure of merit

1. Introduction

The ternary compounds that make up the Delafossite class of oxides have the generic formula ABO_2, where A and B stand for metallic elements. Known for its significant electrical conductivity and transparency in the visible and near-infrared parts of the electromagnetic spectrum, $CuAlO_2$, a well-known derivative of Delafossites, is a p-type semiconductor [1–4].

Delafossite compounds can show electrical conductivity ranging from insulating to semimetallic, depending on the makeup of the compound. Many copper-based Delafossite compounds show good p-type conductivity [5]. The oxides of Delafossite ABO_2 compounds have a layered crystal structure that allows cations to be easily substituted at the A and B sites. This allows for the control of many physical properties of these compounds. These features have enabled Delafossite oxides to be successfully used in various transparent devices, such as pn diodes, UV LEDs, and transparent thin film transistors [5]. Also, some Delafossite materials can exhibit outstanding electrical conductivity, positioning them as appealing contenders for deployment in electronic devices. Some Delafossite variations exhibit magnetic properties, suggesting potential applications in magnetic data storage and other domains. High transparency in the visible and near-infrared ranges is one of the remarkable optical characteristics of several Delafossite compounds, which makes them attractive candidates for

*Corresponding author, E-mail: mohammedelamin.ketfi@univ-msila.dz; saber.saadessaoud@univ-msila.dz

Published online: 12 September 2025

use in solar cells and other optoelectronic devices. Furthermore, their high thermal conductivity holds promise for utilization in electronic device thermal management [6–10]. Delafossite semiconductors are also potential choices for high-speed electronic devices because of their great carrier mobility. Transparent electrodes, photovoltaics, light-emitting diodes, and high-power electronics are among the possible uses for Delafossite semiconductors [11].

To comprehend the electrical and magnetic properties of Delafossites, numerous theoretical studies have been conducted [12].Depending on which A and B ions are used, density functional theory (DFT) computations have shown a variety of electronic band structures, ranging from semiconductors to metals. Moreover, antiferromagnetic ordering has been anticipated by DFT simulations to appear in several Delafossites, including $CuCrO_2$ and $CuFeO_2$ [13], as a result of the coupling of spins to the transition metal ions. Furthermore, an ab initio investigation conducted in 2015 by Ali et al. showed that $CuXO_2$ compounds (where X = Al, Ga, In, B, La, Sc, Y) exhibit semiconductive properties. Understanding the band-edge electrical structure is essential for developing effective photocatalytic materials and uncovering underlying processes. A study uses a unified assessment approach to investigate the relationship between band-edge electronic structure and photocatalytic performance of Delafossite ABO_2 compounds (A = Cu, Ag; B = Al, Ga, In) [14]. Additionally, $PdBO_2$ compounds (B = Al, Cr, and Rh) exhibited semiconducting features in an ab initio research by Ketfi et al. [15].

Experimental investigations into Delafossites have explored the electronic and optical properties of well-known members like $CuAlO_2$, which is distinguished by its high electrical conductivity and optical transparency[16, 17]. Additionally, the photovoltaic properties of Delafossites have been investigated; $CuInO_2$ and $CuGaO_2$ have shown interesting prospects for solar cell applications. Bouich et al. [18] investigated Delafossite as a hole transport layer for perovskite-based solar sales: Based on experimental, and numerical analysis, their XRD outcomes confirmed their hexagonal and rhombohedral structures, with a maximum power conversion efficiency (PCE%) of 22.90.

The energy gap characteristics and value of semiconductors determine their suitability for use in electrical devices. Efficient light emission and absorption can result from direct bandgap semiconductors' increased likelihood of direct electron transitions between energy bands. These semiconductors are so widely used in fiber-optic communication, photovoltaic cells, and other technologies requiring efficient light emission, such as the creation of lasers and bright LED lights for use in displays, lighting, and telecommunications. With remarkable efficiency, they are excellent at transforming electrical energy into light. On the other hand, applications that depend on light emission and absorption are not as successful with indirect semiconductors [19]. However, they are very important in electronic devices such as transistors and thermoelectric devices [20]. Shi et al. used a high-throughput approach based on DFT to explore the Delafossite composition ABX_2. The crystals $KInO_2$, $RbInO_2$, $RbRhO_2$, $CsLaO_2$, $HgMgO_2$, and $BrLaO_2$ are semiconductors with gaps between 3 and 4 eV and relatively low effective masses of approximately $2 \times m_e$(with the notable exception of $RbRhO_2$) [21], since Shi et al., in their investigation [21], only provide structural characteristics like the lattice constants and the atomic positions of the compounds; they did not broaden their investigation to include other features of the Delafossite oxides.

The ability of Delafossite oxides to exhibit p-type semiconductor behavior, superconductivity, and variable electrical conductivity when in contact with some gases (as a result of their reaction with the surface of the Delafossite oxide material) gives them uniqueness and promising industrial demand in many industrial applications, especially in gas sensors, n-p junctions, and optically transparent transistors. The aim of this research is to reveal the advantages of several Delafossite oxides compounds in order to determine their readiness for use in various applications.

2. Computational details

In this work, we employed the Full-Potential Linearized Augmented Plane Wave (FP-LAPW) approach, which is included into the WIEN2k code [22], to examine the structural, optoelectronic, and thermodynamic properties of $CsLaO_2$, $HgMgO_2$, $KInO_2$, and $RbInO_2$, utilizing the principles of density functional theory (DFT). For our calculations, the optimization process involved by Perdew-Burke-Ernzerhof (PBE) formulation for Generalized Gradient Functional (GGA) [19]. Compared to other approximations that use hybrid exchange–correlation functions, such as B3PW, B3LYP [24], and the modified Becke-Johnson exchange (mBJ) approximations, it has been found that the GGA-PBE approximation underestimates the important band gaps. Therefore, the mBJ potential was used for optoelectronic characteristics [25].The unit cell was split into the interstitial space and a set of non-overlapping spherical muffin tins as part of the computational approach. We used plane waves with a cutoff value of $R_{MT} \times K_{MAX} = 9.0$ to expand the wave function in interstitial regions in order to achieve convergence in energy eigenvalues. R_{MT} stands for the minimal muffin-tin radius,

and K_{MAX} is the magnitude of the maximal K vector wave within the Brillouin zone [26]. These chosen computational parameters ensured accurate total energy convergence of 10^{-5} Ry, for electronic and optic properties, meanwhile, in the structural properties, the atomic positions of compounds under study, were adjusted until the force acting on each atom was less than 5×10^{-4} Ry/Bohr. For atoms such as Cs, La, Hg, Mg, K, In, Rb, and O, we employed muffin-tin radii (R_{MT}) of 2.0, 2.1, 2.4, 1.7, 1.9, 2.3, 2.2 and 1.6 atomic units (a.u), respectively. For these elements, we provided the core-valence separation and valence electron configurations. Specifically, Cs ($6s^1$), La ($5d^1\ 6s^2$), Hg ($4f^{14}\ 5d^{10}\ 6s^2$), Mg ($3s^2$), K ($4s^1$), In ($4d^{10}\ 5s^2\ 5p^1$), Rb ($5s^1$), and O ($2s^2\ 2p^4$) have valence electron electronic configurations for Brillouin zone (BZ) integration. To differentiate between valence and core states, we used an energy cutoff of -6.0 eV. Furthermore, we integrated the quasi-harmonic model using the GIBBS2 code [27, 28], which enabled us to take into consideration the impact of temperature and pressure on different thermal properties. We simultaneously used the semi-local Boltzmann transport theory, which was implemented with the help of the BoltzTraP code [29] to estimate the thermoelectric properties.

3. Results and discussion

3.1. Structural properties

In this part, we conducted a study on compounds with the formula ABO_2, where A represents Cs, Hg, K, and Rb, and B represents La, Mg, and In. We analyzed these compounds in their tetragonal phase structure, characterized by the R-3m space group (166), as seen in Fig. 1. Before delving into the computation of lattice constants, bulk modulus, and cohesive energy, it was imperative to ascertain the atomic positions within these compounds via comprehensive geometry optimizations. Using Broyden's approach, the internal locations of the atoms were relaxed by minimizing total energy and force [30, 31].The optimized positions of the constituent atoms of the four compounds under investigation were obtained when the force criterion of 5×10^{-4} Ry/Bohr was satisfied.

To find the unit-cell volume of the most stable state, the total energy for each volume was computed using the Murnaghan equation of state [32]. To ascertain the crystal lattice constants, we also computed the variations in the unit cell's total energy when the c/a crystal lattice ratio changed.

Table 1 provides a comprehensive summary of our findings and offers a comparison with other available data. This table underscores that the (GGA) approach yields satisfactory results for the four compounds: $CsLaO_2$, $HgMgO_2$, $KInO_2$, and $RbInO_2$. The bulk modulus (B) in (GPa) serves as a measure of a material's resistance to deformation caused by hydrostatic pressure. Consequently, the $HgMgO_2$ compound exhibits greater resistance to external pressure, primarily due to the quantity and strength of interatomic bonds it possesses, and therefore, the compound HgMgO2 has bonds that are more resistant to external stress. This observation can be substantiated by utilizing the cohesive energy (E_{coh}), defined as the energy required to break the material into individual atoms and represents the stability of the material in its ground state. The cohesive energy (E_{coh}) is expressed as [33]:

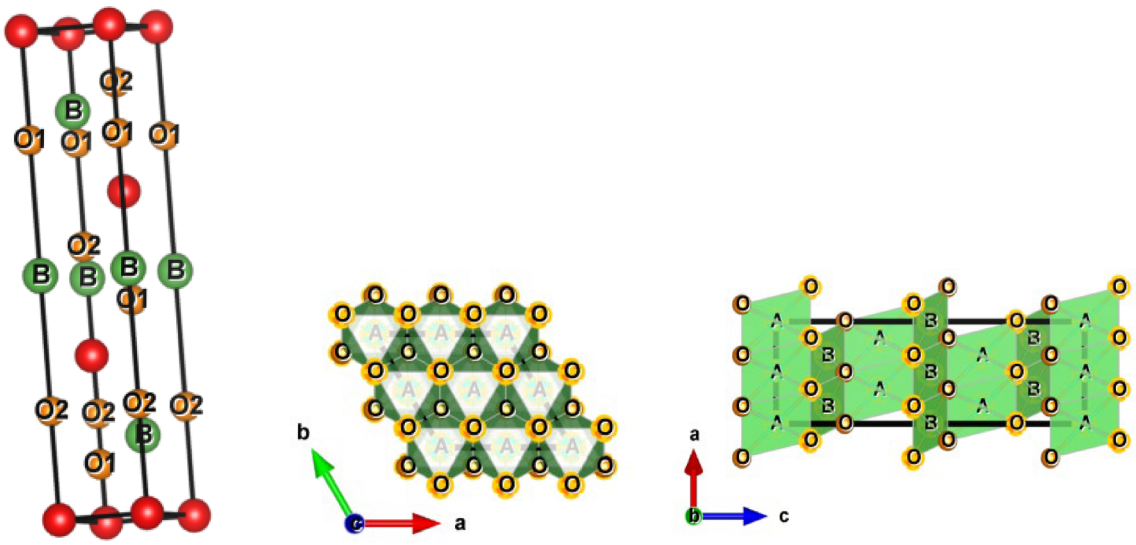

Fig. 1 Crystal Tetragonal structure of ABO_2 compounds

Table 1 The equilibrium lattice constants, bulk modulus, and cohesive energy for $CsLaO_2$, $HgMgO_2$, $KInO_2$, and $RbInO_2$ compounds were computed using GGA-PBE approximations

		a (Å)	c(Å)	B(GPa)	E_{coh}(eV/atom)
$CsLaO_2$	GGA	3,7384	20,5553	82,7368	5.63
	Theo [21]	3,7846	20,8400	–	–
$HgMgO_2$	GGA	3,0700	16,9230	135,7447	1.58
	Theo [21]	3,2590	18,2515	–	–
$KInO_2$	GGA	3,3375	18,4096	108,4334	7.48
	Theo [21]	3,3595	18,5441	–	–
$RbInO_2$	GGA	3,3576	19,1219	103,3103	4.22
	Theo[21]	3,3998	19,3691	–	–

$$E_{coh} = \frac{E_{tot}^{ABO_2} - \left(E_{atom}^{A} + E_{atom}^{B} + 2E_{atom}^{O}\right)}{N_A + N_B + N_O} \quad (1)$$

The total energy $E_{tot}^{ABO_2}$ of the bulk ABO_2 compound is determined based on the quantities of A, B, and O atoms within the unit cell, denoted as N_A, N_B, and N_O respectively. Additionally, $E_{atom}^{A}, E_{atom}^{B}$ and E_{atom}^{O} represent the energies of isolated atoms corresponding to A, B and O. Among these compounds, the second one exhibits the highest cohesive energy, signifying exceptional structural stability. We calculated the cohesive energies for the four compounds: $CsLaO_2$, $HgMgO_2$, $KInO_2$, and $RbInO_2$, the values are shown in Table 1. The calculated cohesion energy section for the four compounds involved in the study indicates that the compound $KInO_2$ is the most cohesive.

3.2. Electronic properties

Delafossite oxides have the potential to be useful in a variety of fields, including electronics, catalysis, and energy conversion. To fully understand and improve the functionality and features of Delafossite oxides and to discover new uses for these materials, it is imperative to investigate their electronic properties.

At high-symmetry locations inside the first Brillouin zone, the energy band structures of the four compounds under study were calculated. Figure 2 reveals distinct behaviors among the four compounds. Remarkably, both $KInO_2$, $RbInO_2$ exhibit large indirect energy gaps of 3.97 eV (Γ-A) and 4 eV (Γ-H). Meanwhile $CsLaO_2$ and $HgMgO_2$ exhibit smaller indirect energy gaps of 2.82 eV (M-L) and 0.3 eV (Γ-A) respectively.

Figure 3 presents a visual representation of the densities of states that were determined through the application of the TB-mBJ approach. In our examination, the studied compounds exhibit a characteristic band structure featuring two distinct bands: a conduction band located above the Fermi level and a valence band positioned below it. These bands are separated by an indirect band gap; with values are 0.3, 2.82, 3.97 and 4.0 eV for $HgMgO_2$, $CsLaO_2$, $KInO_2$ and $RbInO_2$, respectively. Importantly, our band gaps findings for $CsLaO_2$, $KInO_2$ and $RbInO_2$ align excellently with a previous study in reference achieved by Shi et al. [21] with values (4.10, 3.49, and 3.38 eV, respectively) while our gap value for $HgMgO_2$ far away from the previous value (3.25 eV).

As shown in Fig. 3, we looked at the total and partial density of states for atomic orbitals to get insight into the makeup of each band within the band structure spectrum. The lack of state density around the Fermi level indicates that these compounds have semiconductor properties. The "p" orbitals of the Cesium (Cs) atom have a major role in shaping the conduction band of the four ABO_2 compounds in the tetragonal phase structure, while the "s" and "d" orbitals of Cs atoms contribute less significantly. The "s" and "d" orbitals of the Hg and Rb atoms contribute more than this, suggesting significant hybridization in the energy ranges of − 7 eV to 0 eV and 6 eV to 10 eV, respectively.

In $CsLaO_2$, the O-p orbit hybridized with the La-d orbit in the valance band at − 2.0 to − 1.0 eV and with the La-p orbit at − 1.0 to Fermi level. For $HgMgO_2$, the strong hybridization occurs between the O-p orbit and Hg-d orbit at − 7.5 to − 5.0 eV, while weak hybridization occurs between O-p orbit and mixed of Mg-s and Mg-p at − 5.0 to Fermi level. In $KInO_2$, O-p hybridized with In-s and In-p and In-d at the range − 3.5 to − 2.5, − 2.5 to − 0.5, and − 0.5 to 0, respectively. In $RbInO_2$, O-p hybridized strongly with In-s and In-d at the range − 3.5 to − 2.5 eV, and − 0.5 to 0 respectively, while it hybridized weakly with In-d at the range − 2.5 to − 0.5 eV.

3.3. Optical properties

Delafossite compounds are useful in several fields such as optoelectronics, photocatalysis, and catalysis because of their wide range of fascinating optical properties [34]. The bandgap energy of ABO_2 compounds is one of its most important optical characteristics, determining both their optical transparency and absorption of light. ABO_2 compounds' composition and crystal structure can be changed to change their bandgap energy, making them adaptable for a range of uses [35, 36].

To explore the real and imaginary components $\varepsilon_1(\omega)$ and $\varepsilon_2(\omega)$, which are computed using the formula [37–40], we used the dielectric complex function $\varepsilon(\omega)$:

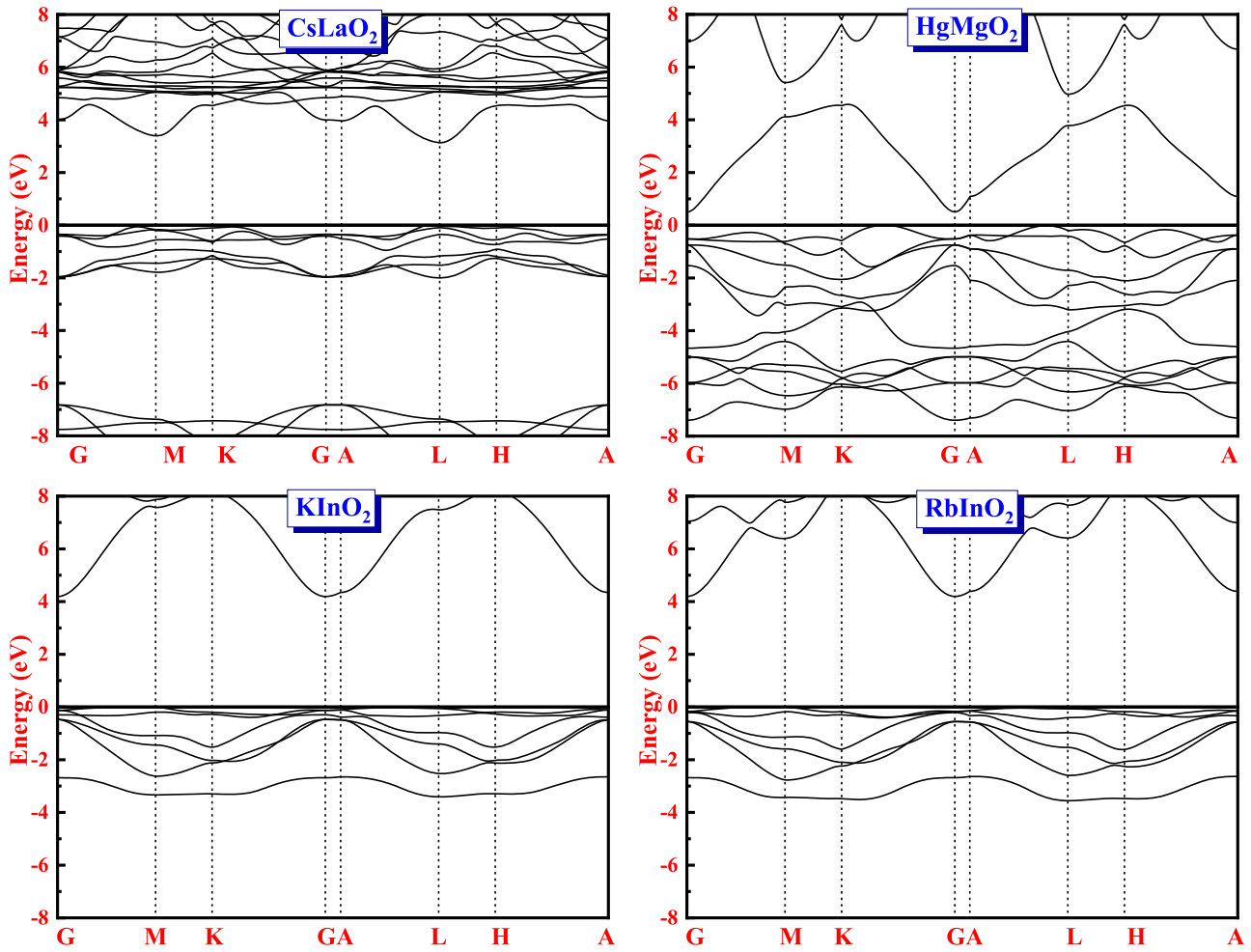

Fig. 2 Band structure curves for $CsLaO_2$, $HgMgO_2$, $KInO_2$, and $RbInO_2$ using the TB-mBJ approximation

$$\varepsilon(\omega) = \varepsilon_1(\omega) + i\varepsilon_2(\omega) \quad (2)$$

The real component of the dielectric function $\varepsilon_1(\omega)$ provides insight into how the material interacts with incident photons, revealing the dispersion characteristics of its constituent elements [41]. Moreover, it provides important details about the material's electrical polarizability state [42]. On the other hand, the energy absorbed by the material is represented by the imaginary component of the dielectric function, $\varepsilon_2(\omega)$. The electronic band structure is used to determine this imaginary component $\varepsilon_2(\omega)$, which is the evaluation of momentum matrix elements between occupied and unoccupied electronic states. Conversely, the Kramers–Kronig transformation can be used to obtain the real component from $\varepsilon_2(\omega)$ [43].

Using the TB-mBJ approximation, we computed both the imaginary and real parts of the dielectric functions of the compounds under investigation in the x, y, and z directions. Figure 4 provides important information on the values of the static dielectric constant, which is the real dielectric constant at zero frequency, or $\varepsilon_1(0)$. One noteworthy finding from Fig. 4 is that, in comparison to the other compounds, $HgMgO_2$ has a much higher static dielectric constant value ($\varepsilon_1(0) \approx 60$). It's worth noting that this value serves as an indicator of the material's response to an external electric field. However, we notice that the $\varepsilon_1(\omega)$ spectrum experiences a rapid rise from its static dielectric constant value $\varepsilon_1(0)$. At specific energy levels, namely 2.95 eV, 0.62 eV, and 9 eV for $CsLaO_2$, $HgMgO_2$, $KInO_2$ and $RbInO_2$ respectively, the spectrum reaches its peak.

It is important to highlight that as we move through the range of 1–14 eV for the four compounds under investigation, the $\varepsilon_1(\omega)$ values gradually decrease and eventually become negative. This transition in behavior signifies a shift toward metallic characteristics within this energy range.

$\varepsilon_2(\omega)$, as depicted in Fig. 4, we can discern the optical band gaps for $CsLaO_2$, $HgMgO_2$, $KInO_2$, and $RbInO_2$,

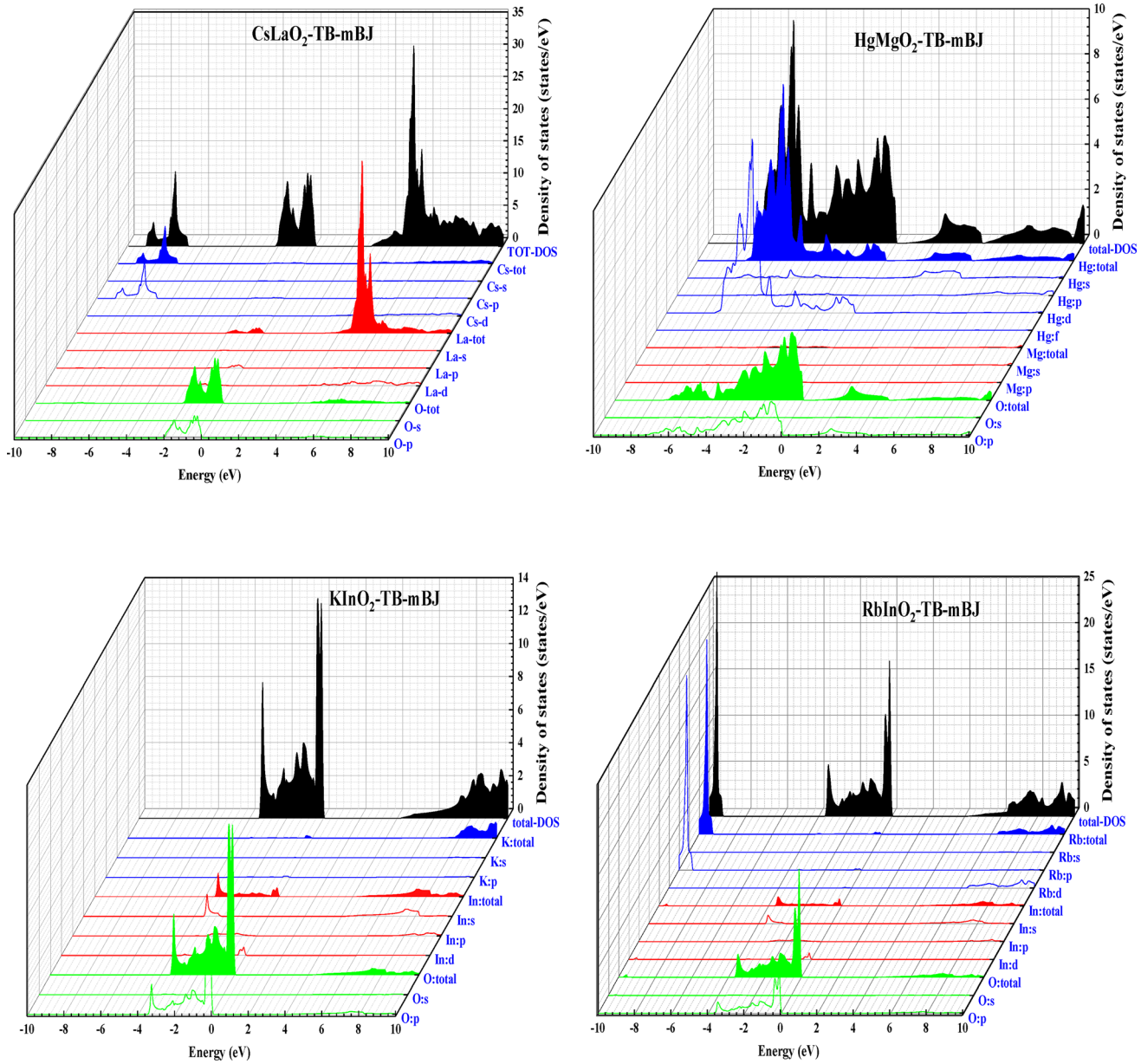

Fig. 3 The calculated total and partial density of states for $CsLaO_2$, $HgMgO_2$, $KInO_2$, and $RbInO_2$within the TB-mBJ approximation

which have been determined as 2.82 eV, 0.29 eV, 3.97 eV, and 4 eV, respectively. Using the TB-mBJ approximation, these values are retrieved from the imaginary component of the dielectric function.

The absorption coefficient α(ω) is related to the extinction coefficient k(ω) through the following equation [44]:

$$\alpha(\omega) = (4\pi/\lambda)\mathrm{k}(\omega) \tag{3}$$

In this context, The wavelength of light in a vacuum, given by λ, can be found using the dielectric function and the following correlation[45]:

$$\alpha(\omega) = \frac{2\pi\omega}{c}\sqrt{\frac{-R_e(\varepsilon(\omega)|\varepsilon(\omega)|)}{2}} \tag{4}$$

The absorption edge is sited at approximately 2.82 eV for $CsLaO_2$, 0.29 eV for $HgMgO_2$, 3.97 eV for $KInO_2$, and 4 eV for $RbInO_2$. In the specified energy ranges, all four compounds exhibit pronounced responses to incident photons, specifically within the intervals of 3 to 14 eV for $CsLaO_2$, 1 to 14 eV for $HgMgO_2$, and 9–18 eV for both $KInO_2$ and $RbInO_2$.

We introduce another parameter known as the reflective coefficient, denoted as R(ω). This parameter quantifies the portion of energy that is reflected from the surface of the

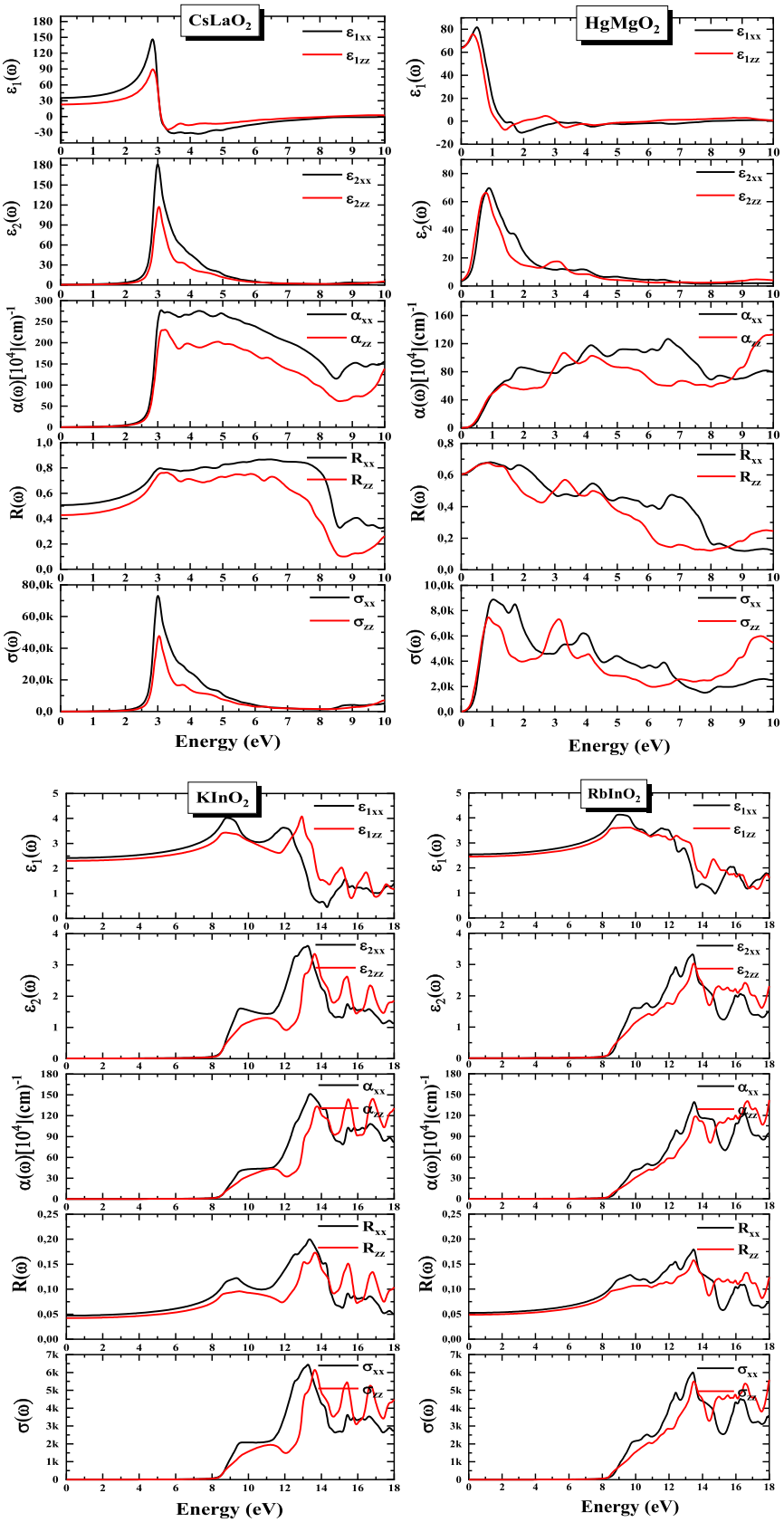

Fig. 4 Optical properties of $CsLaO_2$, $HgMgO_2$, $KInO_2$, and $RbInO_2$ within TB-mBJ approach

solid and can be calculated using the refractive index as outlined below [46]:

$$R(\omega) = \left| \frac{(n(\omega)-1)^2 + k(\omega)^2}{(n(\omega)+1)^2 + k(\omega)^2} \right| \quad (5)$$

Figure 4 illustrates that the zero-frequency reflectivity limit, R(0), for ABO_2 is determined to be 50% for $CsLaO_2$, 60% for $HgMgO_2$, and 5% for both $KInO_2$ and $RbInO_2$. Additionally, prominent reflection peaks are observed at energy levels of 6.3 eV, 1 eV, 13,5 eV and 13.5 eV for all four compounds, aligning with the negative values of $\varepsilon_1(\omega)$.

Moreover, the definition of optical conductivity is given by the following formula [39]:

$$\sigma(\omega) = -(i\omega/4\pi)\varepsilon(\omega) \quad (6)$$

The optical conductivity for $CsLaO_2$, $HgMgO_2$, $KInO_2$, and $RbInO_2$ is displayed in Fig. 4 at 2.82 eV, 0.29 eV, 3.97 eV, and 4 eV, respectively. Note that the maximum optical conductivity value is at 3 eV for $CsLaO_2$, 1 eV for $HgMgO_2$and 13 eV for both $KInO_2$ and $RbInO_2$.

3.4. Thermodynamic properties

A thorough understanding of the thermal properties of the materials used in solar energy systems is essential for achieving optimal performance. This understanding should encompass how these properties are influenced by alterations in temperature and pressure. It is critical to thoroughly examine a material's ability to change its energy absorption, coefficient of thermal expansion, resistance to deformation, and other relevant properties.

Theoretical investigation of these features was conducted over a temperature range of 1000 units, and the influence of pressures up to 30 GPa was considered. This analysis was performed using the quasi-harmonic Debye model, implemented within the GIBBS2 code [27, 28]. The Gibbs free energy expression was used to study how changes in temperature and pressure affect the thermodynamic properties of the solid material.

$$G^*(x,V;P,T) = E_{stat}(x,V) + PV + A^*_{vib}(x,V;T) + F^*_{el}(x,V;T) \quad (7)$$

Non-equilibrium vibrational Helmholtz free energies are denoted in this context by A^*_{vib} *and* F^*_{el}, respectively, representing electronic and vibrational free energies. The hydrostatic situation is symbolized by the word PV, while E_{stat} represents the total energy. Debye's model can be used to determine the non-equilibrium vibrational Helmholtz free energy, A^*_{vib}, in relation to the vibrational density of states g(ω), which is also referred to as the density of phonon states:

$$A^*_{vib} = \int_0^\infty \left[\frac{\omega}{2} + k_B T \, \mathrm{Ln}(1 - e^{-\frac{\omega}{k_B T}}) \right] g(\omega) d\omega \quad (8)$$

$$F^*(x,V;T) = E_{stat}(x,V) + A^*_{vib}(x,V;T) \quad (9)$$

Under constant pressure and temperature conditions, we achieve the equilibrium state by minimizing the Gibbs free energy G* concerning volume.

$$\left(\frac{\partial G^*(V,P,T)}{\partial V} \right)_{P,T} = 0 \quad (10)$$

To derive formulas for various thermal parameters, including entropy (S), heat capacity at constant volume (C_v), and the coefficient of thermal expansion (α), our initial step involves solving the final equation.

$$S = -3nk_B \ln(1 - e^{-\theta_D/T}) + 4nk_B D(\theta_D/T) \quad (11)$$

$$C_v = 12nk_B D(\theta_D/T) - \frac{9nk_B \theta_D/T}{e^{\theta_D/T} - 1} \quad (12)$$

The term D (θ/T) represents the Debye integral, with 'n' indicating the number of atoms per unit volume. This expression is formulated as follows:

$$D(x) = \frac{3}{x^3} \int_0^x \frac{y^3 e^{-y}}{1 - e^{-y}} dy \quad (13)$$

$$\alpha = -\frac{1}{V} \left(\frac{\partial V}{\partial T} \right)_P = \frac{\gamma C_V}{V B_T} \quad (14)$$

The heat capacity at constant volume (C_v), as expressed in formula (13), measures the value of energy that a substance can absorb per mole when its temperature rises by 1.0 K. In Fig. 5, we visualize the variation in ABO_2's heat capacity with respect to temperature at a pressure of P = 0. The graph in Fig. 5 demonstrates the behavior of C_v concerning temperature. At low temperatures (below 200 K), C_v exhibits an exponential increase, roughly proportional to T^3. However, it stabilizes at approximately 100 J/molK when the temperature reaches or exceeds 450 K, adhering to the Petit-Dulong law [47].

Entropy, a thermal term that symbolizes the irreversible energy in a system, is plotted in Fig. 5b. According to the data, $CsLaO_2$ has a higher entropy value than the other compounds. Moreover, the quasi-linear growth patterns of all four entropy curves show independent changes in temperature and pressure. This tendency can be clarified through the fact that as temperatures increase, more vibrational modes are produced, which increases the number of potential configurations. On the other hand, as pressure rises, atomic motion is constrained, which lowers vibrational entropy.

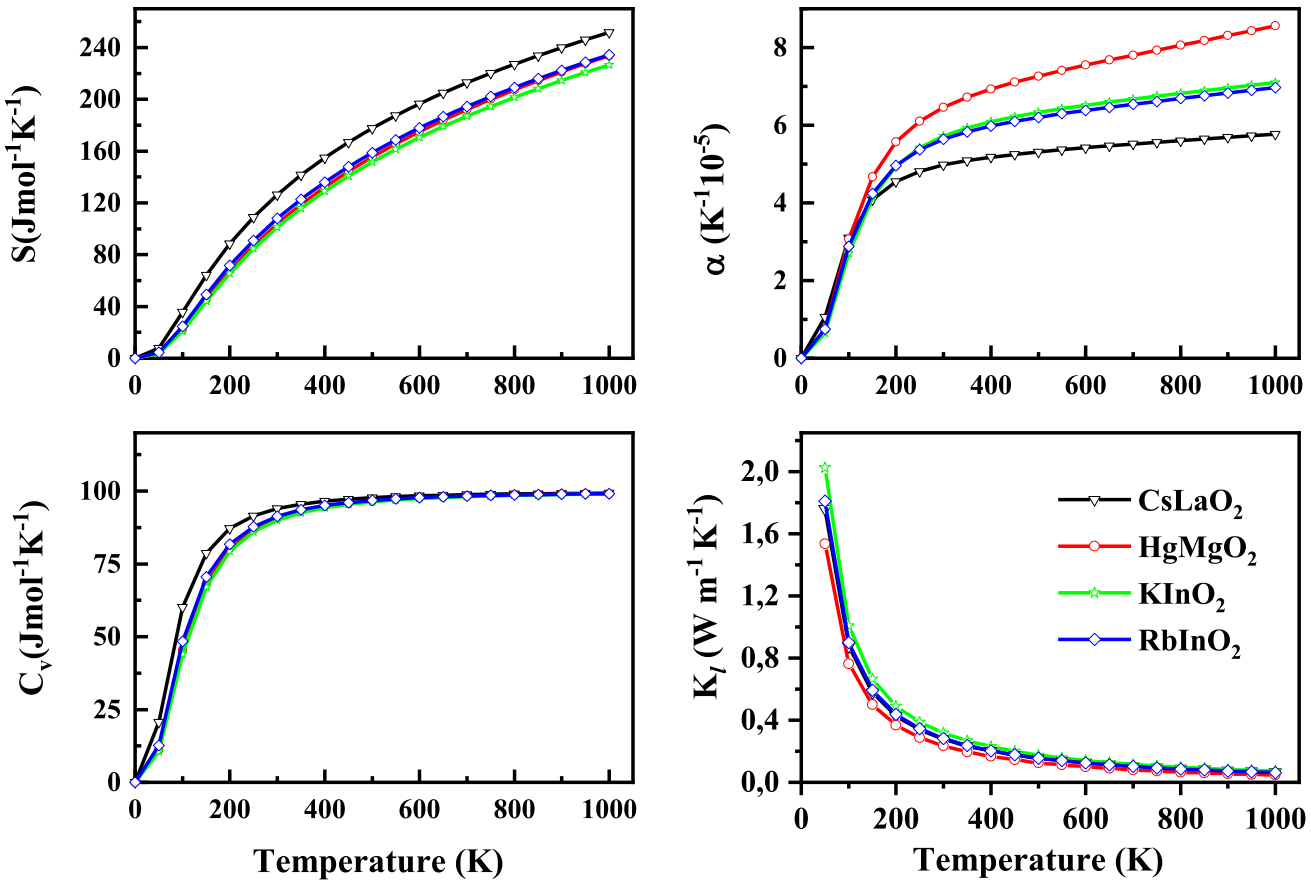

Fig. 5 Heat capacity (C_V), entropy (S), thermal expansion (α) and lattice thermal conductivity (K_l) of $CsLaO_2$, $HgMgO_2$, $KInO_2$, and $RbInO_2$ Delafossite compounds vary with temperature at 0 GPa pressure

Thermal expansion, which signifies the fractional change in volume of a substance as temperature varies, is influenced by increased atomic mobility due to temperature changes. The main elements affecting thermal expansion (α) are the substance's nature, the quantity of bonds, atoms, and structural features. The relationship between α and temperature is illustrated in Fig. 5.

The graph in this section shows that all of the compounds that are being studied expand quickly at temperatures below 200 K and gradually at temperatures that are equal to or higher than 200 K. Furthermore, the compound $HgMgO_2$ clearly shows the highest α at temperatures below 350 K, while at temperatures above 350 K, it shows a higher thermal expansion value than the other compounds.

To estimate the lattice thermal conductivity we adopt Slack model formula given as [48]:

$$K_l = \frac{A\vartheta_D^3 V^{1/3} m}{\gamma^2 n^{2/3} T} \tag{15}$$

where A is a physical constant equal to $A = \frac{2.4310^{-8}}{1-\frac{0.514}{\gamma}+\frac{0.228}{\gamma^2}}$ and ϑ_D, γ, V, n andm are the Debye temperature, Grüneisen parameter, the volume per atom, the number of atoms in the primitive unit cell and m is the average mass of all the atoms in the crystal respectively).

From the curve depicting the dependence of crystalline heat conductivity on temperature for the four compounds under study, it is evident that the contribution of the crystalline lattice to heat transfer at low temperatures (below 200 Kelvin) is moderate, averaging around 1 $Wm^{-1}K^{-1}$ at 100 K. However, it approaches its minimum level (0.02 $Wm^{-1}K^{-1}$) at temperatures above 300.

3.5. Thermoelectric properties

Thermoelectric materials enable the direct conversion of thermal energy into electricity. Delafossite materials, which efficiently convert heat to electricity and have outstanding heat absorption capabilities, show significant promise for this application. The thermoelectric properties of these compounds are estimated using Boltzmann transport theory with the BoltzTraP program [14], providing the final values. However, the ZT figure of merit measures the current conversion efficiency of thermoelectric devices, which is relatively low. The term ZT is defined as follows:

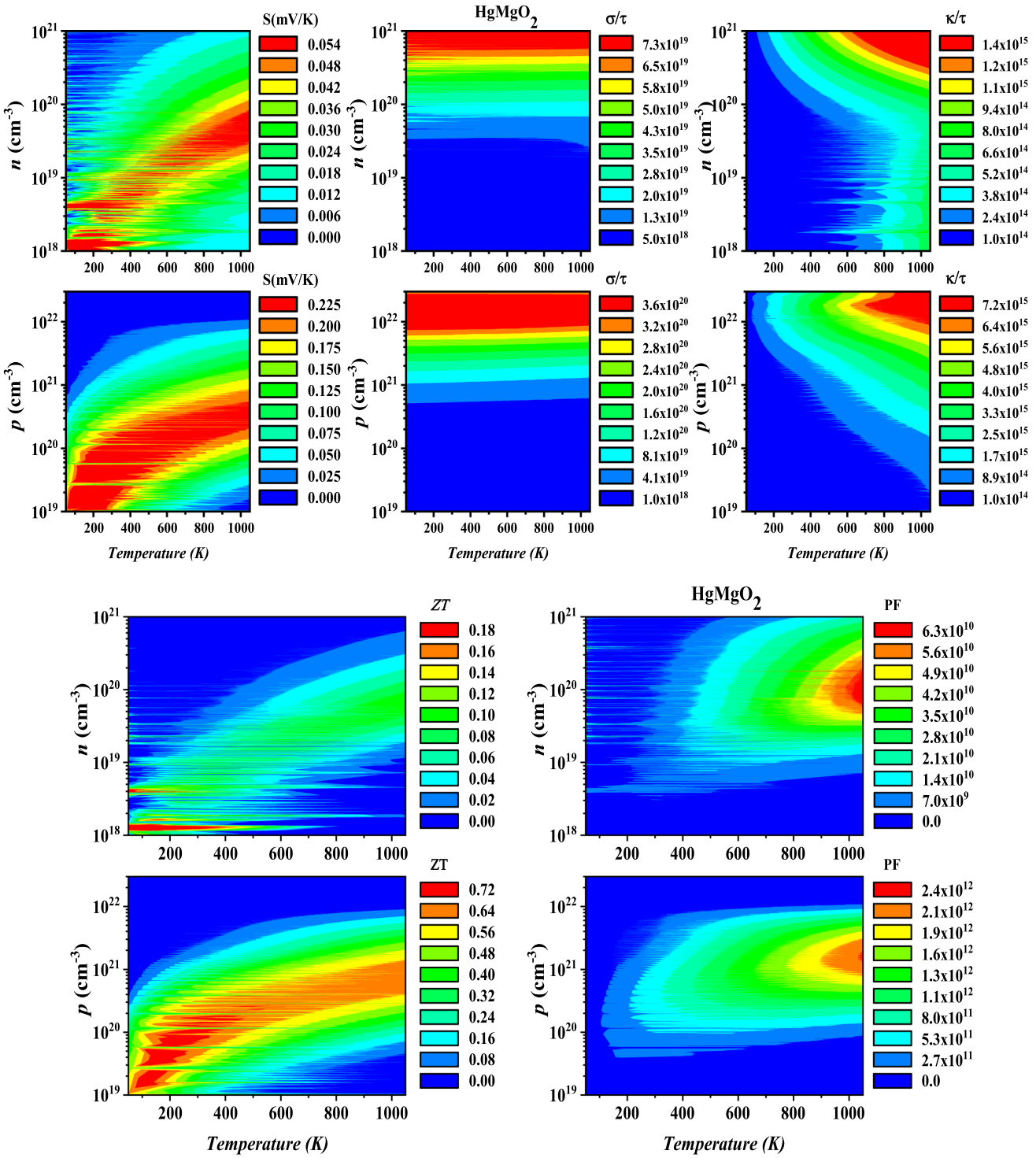

Fig. 6 Changes in the Seebeck coefficient (S), electrical conductivity (σ/τ), electronic thermal conductivity (κ/τ), figure of merit (ZT), and power factor (PF) for $HgMgO_2$ compound as a function of electrons and holes concentrations and temperature

$$ZT = S^2 \frac{\sigma T}{k} \tag{16}$$

where S is the Seebeck coefficient, σ is the electrical conductivity, $\kappa = \kappa_e + \kappa_l$ is the total thermal conductivity and T is the absolute temperature.

The inherent Seebeck coefficient of a material describes the relationship between the voltage across its terminals and the applied temperature gradient. This temperature disparity drives the movement of charge carriers inside the material, such as electrons or holes [6, 29], resulting in the generation of an electric current. This part investigated the bulk of the thermoelectric properties, including how they change with the concentration of each type of charge carrier (electrons and holes) over a temperature range of up to 1000 K.

Concerning the Seebeck coefficient (S) for the four compounds, the results obtained in Fig. 6 for the $HgMgO_2$ compound indicate that increasing the temperature above 600 K results in a higher Seebeck coefficient for both electrons and holes, surpassing 0.3 mV/K. Furthermore, increasing the concentration of charge carriers raises the Seebeck value for holes while decreasing it for electrons.

The electrical and thermal conductivity of electrons and holes were used to investigate charge carriers' contributions to thermal and electrical conductivity. At room temperature, the electrical conductivity of holes exceeds that of electrons, with values reaching $3.7 \times 10^{20}\ \Omega^{-1}cm^{-1}$ for the $HgMgO_2$ combination doped with $10^{21}\ cm^{-3}$ electrons. For both electrons and holes, thermal conductivity increases as temperature rises.

The figure of merit and power factor are two critical parameters that evaluate materials' performance in thermoelectric conversion. They also provide details on a variety of charge carriers and optimal doping concentrations for materials, in addition to the optimal thermal conditions for high efficiency. The plots showing variations in the figure of merit and power factor indicate that holes have better thermoelectric characteristics than electrons. Doping, also known $HgMgO_2$ with a concentration of 10^{22} cm^{-3} can achieve a figure of merit of up to 0.8 as a power factor of over $2.2 \times 10^{12}\ W.cm^{-1}.s^{-1}.K^{-2}$. Based on these data, it is possible to deduce that the four compounds are more suitable for hole doping (p-type) due to their comparatively weak thermoelectric properties.

4. Conclusion

In this work, we evaluated the electrical, optical, and structural characteristics of tetragonal phase Delafossite semiconductors, namely $CsLaO_2$, $HgMgO_2$, $KInO_2$, and $RbInO_2$, using DFT calculations. According to our research, all four compounds show semiconductor activity, however with different energy band gaps. $KInO_2$ and $CsLaO_2$ in particular show favorable cohesive energies, indicating stable structures. Furthermore, our study of their optical properties revealed favorable properties for all compounds, with the maximum absorption coefficient being shown by $CsLaO_2$. Together, these discoveries provide insightful information about the characteristics of these Delafossite semiconductors and their prospective uses in a variety of fields. Our results suggest that ABO_2 compounds have good thermodynamic and electrical properties, which make them promising for usage in electro-optical domains and related applications. Notably, their high Seebeck coefficient and low thermal conductivity considerably increase their figure of merit, bringing it close to unity. These findings provide useful guidance for future efforts aimed at enhancing the performance of such materials through compositional tuning or structural optimization. Furthermore, our findings indicate that these four compounds have potential for thermoelectric applications, as evidenced by an assessment of their thermoelectric properties using the semi-classical Boltzmann theory. In a broader sense, our findings are consistent with earlier theoretical investigations, supporting the potential value of these chemicals in a variety of applications.

Author contributions MEK: Conceptualization, Methodology, Formal analysis, Writing and Investigation, SSE: Verification, Supervision, Visualization, Conceptualization. Writing, SAA: Verification, Supervision, Visualization and Writing, AYA-R: Supervision, Visualization.

Funding No funding was received to assist with the preparation of this manuscript.

Availability of data and materials All the associated data with this study is present in the manuscript.

Declarations

Competing interests There is no conflict of interest.

Ethical approval There is no ethical approval required for this research work.

References

[1] A V Chadwick, A N Blacklocks, A Rougier and C Yaicle *J. Phys. Conf. Ser.* **249** 5012045 (2010).
[2] M A Gillispie *Doctor of Philosophy* (Iowa State University, Digital Repository, Ames) (2006).
[3] M Khedidji, F Saib, O Mahroua and M Trari *J. Mater. Sci. Mater. Electron.* **33** 26474 (2022).
[4] M Khedidji, F Saib and M Trari *Vacuum* **222** 113099 (2024).
[5] M A Marquardt, N A Ashmore, and D P Cann *Proc. Fourth Int. Symp. Transparent Oxide Thin Films Electron. Opt. TOEO-4* **496** 146 (2006).
[6] S Akin, F Sadegh, S Turan, S Sonmezoglu and A C S Appl *Mater. Interfaces* **11** 45142 (2019).
[7] E-H Lee, E-B Kim, M S Akhtar and S Ameen *Ceram. Int.* **48** 16667 (2022).
[8] R Venkatasubramanian, E Siivola, T Colpitts and B O'quinn *Nature* **413** 597 (2001).

[9] N M A Palumbo (2013).
[10] I Sinnarasa, Y Thimont, L Presmanes, C Bonningue, A Barnabé and P Tailhades *Appl. Surf. Sci.* **455** 244 (2018).
[11] H N Abdelhamid *Mater. Sci. Forum* **832** 28 (2015).
[12] K Ismail, G Murtaza, S Tahir, G Nazir, N A Kattan, H Albalawi, B U Haq and M Morsi *J. Solid State Chem.* **314** 123432 (2022).
[13] M Moreira, J Afonso, J Crepelliere, D Lenoble and P Lunca-Popa *J. Mater. Sci.* **57** 3114 (2022).
[14] S-W Fu, J Yang, Z-Y Zhao, B-F Shan, J-X Zhang, J Zhang, Q Liu, J Feng, Z Li and Z Zou *Chem. Mater.* **36** 3177 (2024).
[15] M E Ketfi and S S Essaoud *Quantum Electron.* **55** 1013 (2023).
[16] N Zhang, J Sun and H Gong *Coatings* **9** 137 (2019).
[17] M Khedidji, H Yousfi, F Saib and M Trari *Solid State Commun.* **394** 115733 (2024).
[18] A Bouich, J C Torres, H Chfii, J Marí-Guaita, Y H Khattak, F Baig, B M Soucase and P Palacios *Sol. Energy* **250** 18 (2023).
[19] S S Essaoud, S M Azar, A A Mousa and A Y Al-Reyahi *Phys. Scr.* **98** 075930 (2023).
[20] S K Maurya, H R Galvan, G Gautam and X Xu *Energies* **15** 8698 (2022).
[21] J Shi, T F T Cerqueira, W Cui, F Nogueira, S Botti and M A L Marques *Sci. Rep.* **7** 43179 (2017).
[22] P Blaha, K Schwarz, F Tran, R Laskowski, G K H Madsen and L D Marks *J. Chem. Phys.* **152** 074101 (2020).
[23] J P Perdew, K Burke and M Ernzerhof *Phys. Rev. Lett.* **77** 3865 (1996).
[24] R I Eglitis and R Jia *Materials* **16** 7623 (2023).
[25] A D Becke and E R Johnson *J. Chem. Phys.* **124** 221101 (2006).
[26] H J Monkhorst and J D Pack *Phys. Rev. B* **13** 5188 (1976).
[27] A Otero-de-la-Roza, D Abbasi-Pérez and V Luaña *Comput. Phys. Commun.* **182** 2232 (2011).
[28] A Otero-de-la-Roza and V Luaña *Comput. Phys. Commun.* **182** 1708 (2011).
[29] G K H Madsen and D J Singh *Comput. Phys. Commun.* **175** 67 (2006).
[30] C G Broyden *IMA J. Appl. Math.* **6** 76 (1970).
[31] C G Broyden *IMA J. Appl. Math.* **6** 222 (1970).
[32] F D Murnaghan *Proc. Natl. Acad. Sci.* **30** 244 (1944).
[33] M E Ketfi, S S Essaoud, S M Al Azar, A Y Al-Reyahi, A A Mousa and N Al-Aqtash *Phys. Scr.* **99** 015908 (2024).
[34] X Huang and E Meggers *Acc. Chem. Res.* **52** 833 (2019).
[35] S Singh, A K Tangra and G S Lotey *Electron. Mater. Lett.* **14** 594 (2018).
[36] M E Ketfi, S S Essaoud, S Al Azar, and A Y Al-Reyahi *J. Inorg. Organomet. Polym. Mater.* (2024).
[37] M Gajdoš, K Hummer, G Kresse, J Furthmüller and F Bechstedt *Phys. Rev. B* **73** 045112 (2006).
[38] M A Khan, A Kashyap, A K Solanki, T Nautiyal and S Auluck *Phys. Rev. B* **48** 16974 (1993).
[39] C Ambrosch-Draxl and J O Sofo (2004).
[40] S Kataria, H Mudila, A Kumar and P Prasher *Nanosci. Nanotechnol.-Asia* **12** 10474 (2022).
[41] B Ul Haq, S AlFaify, A S Jbara, R Ahmed, F K Butt, A Laref, A R Chaudhry and Z A Shah *Ceram. Int.* **46** 22181 (2020).
[42] S S Essaoud, A Bouhemadou, M E Ketfi, M Radjai and D Allali *Chem. Phys. Lett.* **850** 141455 (2024).
[43] S Saad Essaoud, A Bouhemadou, M Radjai, M Elamin Ketfi, D Allali, S Bin-Omran and S Maabed *Inorg. Chem. Commun.* **159** 111733 (2024).
[44] S Sâad Essaoud, A Bouhemadou, M E Ketfi, D Allali and S Bin-Omran *Phys. B Condens. Matter* **657** 414809 (2023).
[45] A Y Al-Reyahi, A Mufleh, S M Al Azar, M Maghrabi, N Al Aqtash, S S Essaoud, K Berarma, A Shaheen, M E Ketfi and A A Mousa *Solid State Sci.* **148** 107435 (2024).
[46] S Saad Essaoud, A Bouhemadou, D Allali, M E Ketfi, M Radjai and S Bin-Omran *J. Inorg. Organomet. Polym. Mater.* **34** 885 (2024).
[47] Mm Petit and Dulong *Philos. Mag.* **54** 267 (1819).
[48] G A Slack *J. Phys. Chem. Solids* **34** 321 (1973).